

Article

# Oxygen Reduction Reaction and Hydrogen Evolution Reaction Catalyzed by Pd–Ru Nanoparticles Encapsulated in Porous Carbon Nanosheets

Juntai Tian <sup>1,†</sup>, Wen Wu <sup>1,†</sup>, Zhenghua Tang <sup>1,2,\*</sup> , Yuan Wu <sup>3</sup>, Robert Burns <sup>4</sup>,  
Brandon Tichnell <sup>4</sup> , Zhen Liu <sup>4</sup> and Shaowei Chen <sup>1,5</sup> 

<sup>1</sup> Guangzhou Key Laboratory for Surface Chemistry of Energy Materials, New Energy Research Institute, School of Environment and Energy, South China University of Technology, Guangzhou Higher Education Mega Centre, Guangzhou 510006, China; tianjuntai2523@163.com (J.T.); wuwen0730@163.com (W.W.); shaowei@ucsc.edu (S.C.)

<sup>2</sup> Guangdong Provincial Key Laboratory of Atmospheric Environment and Pollution Control, Guangdong Provincial Engineering and Technology Research Center for Environmental Risk Prevention and Emergency Disposal, South China University of Technology, Guangzhou Higher Education Mega Centre, Guangzhou 510006, China

<sup>3</sup> Department of Clinical Medicine, Fuzhou Medical College of Nanchang University, Fuzhou 344000, China; wuwyuankx12@163.com

<sup>4</sup> Department of Physics & Engineering, Frostburg State University, Frostburg, MD 21532–2303, USA; rsburns0@frostburg.edu (R.B.); btichnell0@frostburg.edu (B.T.); Zhenliu8@gmail.com (Z.L.)

<sup>5</sup> Department of Chemistry and Biochemistry, University of California, 1156 High Street, Santa Cruz, California, CA 95064, USA

\* Correspondence: zhht@scut.edu.cn; Tel.: +86-20-39381200

† These authors contributed equally.

Received: 7 July 2018; Accepted: 2 August 2018; Published: 11 August 2018



**Abstract:** Developing bi-functional electrocatalysts for both oxygen reduction reaction (ORR) and hydrogen evolution reaction (HER) is crucial for enhancing the energy transfer efficiency of metal–air batteries and fuel cells, as well as producing hydrogen with a high purity. Herein, a series of Pd–Ru alloyed nanoparticles encapsulated in porous carbon nanosheets (CNs) were synthesized and employed as a bifunctional electrocatalyst for both ORR and HER. The TEM measurements showed that Pd–Ru nanoparticles, with a size of approximately 1–5 nm, were uniformly dispersed on the carbon nanosheets. The crystal and electronic structures of the Pd<sub>x</sub>Ru<sub>100–x</sub>/CNs series were revealed by powder X-ray diffraction (XRD) and X-ray photoelectron spectroscopy (XPS). The as-prepared samples exhibited effective ORR activity in alkaline media and excellent HER activity in both alkaline and acid solutions. The Pd<sub>50</sub>Ru<sub>50</sub>/CNs sample displayed the best activity and stability among the series, which is comparable and superior to that of commercial 10% Pd/C. For ORR, the Pd<sub>50</sub>Ru<sub>50</sub>/CNs catalyst exhibited an onset potential of 0.903 V vs. RHE (Reversible Hydrogen Electrode) and 11.4% decrease of the current density after 30,000 s of continuous operation in stability test. For HER, the Pd<sub>50</sub>Ru<sub>50</sub>/CNs catalyst displayed an overpotential of 37.3 mV and 45.1 mV at 10 mA cm<sup>–2</sup> in 0.1 M KOH and 0.5 M H<sub>2</sub>SO<sub>4</sub>, respectively. The strategy for encapsulating bimetallic alloys within porous carbon materials is promising for fabricating sustainable energy toward electrocatalysts with multiple electrocatalytic activities for energy related applications.

**Keywords:** Pd–Ru alloys; porous carbon nanosheets; bifunctional electrocatalyst; oxygen electroreduction; hydrogen evolution reaction

## 1. Introduction

To resolve the increasing global energy crisis and the associated environmental problems, a great deal of research attention has been paid to developing alternative green energy conversion and storage technologies, including water splitting, fuel cells, and metal–air batteries in the past decade [1–4]. The oxygen reduction reaction (ORR) is the reaction occurring at the cathode, which governs the energy transfer efficiency of metal–air batteries and fuel cells, while the hydrogen evolution reaction (HER) is probably one of the most effective approaches to producing pure hydrogen massively. At present, the platinum-based materials have been widely considered as the state-of-art catalysts for both ORR and HER [5–7]. However, their rarity and accompanying high cost pose a serious limitation for large-scale applications [7–9]. Furthermore, platinum-based catalysts displayed poor long-term electrochemical stability. Therefore, developing non-Pt based earth-abundant materials with a desirable efficiency and ideal longevity as a catalyst for both ORR and HER is of great importance, and has potential practical values for water splitting, metal–air batteries, fuel cells, and other renewable energy devices [5,7,10].

Recently, palladium-based catalysts have aroused wide concern among researchers, because of their similar nature to platinum (in the same group of the periodic table, same crystal structure, and similar atomic size) [11]. Moreover, palladium is about 50 times more abundant on Earth than platinum, hence, its price is lower than that of platinum [11]. Therefore, Pd has been regarded as a promising substitution for Pt. To further enhance the intrinsic activity and reduce the cost, alloying palladium with other metals to form bimetallic alloys have been demonstrated as one of the most effective approaches to fabricate catalysts with high efficiency and robust stability [12,13]. Note that the bimetallic alloys possess the so-named synergistic effects in the catalytic process; on one hand, the introduction of another metal can generate certain geometric configuration, which is called the ensemble effect, and on the other hand, the altered electronic structure induced by hetero metal–metal bond is favorable for the activation of the catalyst [14,15]. A variety of Pd alloys, including PdAu [16–18], PdAg [19–21], PdRh [22], PdNi [23,24], PdCo [25,26], PdCu [27], and PdSn [28] have demonstrated higher ORR activities and enhanced long-term stabilities than the pure Pd-based catalysts.

Among all kinds of metals as substrate to alloy palladium, ruthenium is a special one that has attracted our attention, based on the following factors. First of all, on the left of the periodic table of palladium, ruthenium possesses some free states around the Pd Fermi level, which makes it readily able to form stable alloys with palladium [29]. Secondly, ruthenium bears a high earth abundance and hence is much cheaper than other noble metals. Finally, and most importantly, recent studies have shown that ruthenium has excellent electrocatalytic capability, especially for HER. For instance, the Chen group found that when ruthenium ions were embedded into the molecular skeletons of graphitic carbon nitride ( $C_3N_4$ ) nanosheets, an excellent HER performance can be obtained, with an overpotential of only 140 mV, to achieve the current density of  $10 \text{ mA cm}^{-2}$ , a low Tafel slope of  $57 \text{ mV dec}^{-1}$ , and a large exchange current density of  $0.072 \text{ mA cm}^{-2}$  [30]. In another study, singly dispersed Ru atoms chelated to a nitrogen doped carbon matrix were prepared by Zhang et. al., and the resultant Ru/NC electrocatalyst exhibited excellent electrocatalytic HER activity with an extremely low overpotential of only 21 mV at  $10 \text{ mA cm}^{-2}$  [31]. Recently, the Qiao group developed an anomalous ruthenium catalyst that showed a 2.5 times higher hydrogen generation rate than Pt in the alkaline solutions, and density functional theory computation revealed that the high activity of the anomalous Ru catalyst originated from its suitable adsorption energies to some key reaction intermediates and reaction kinetics in the HER process [32]. Employing the synergy of palladium and ruthenium to improve the catalytic activity as electrocatalysts has been widely reported. R. R. Adzic et al. synthesized Pd monolayers supported on a Ru (0001) catalyst for ORR, which holds a half-wave potential of  $\sim 0.45 \text{ V vs. RHE}$  [33]. In another study, the Lee group synthesized a series of carbon supported  $Pd_xRu$  ( $x = 1, 3, 9$ ) nanoparticles for ORR in  $0.1 \text{ M HClO}_4$ , and the as-formed  $Pd_9Ru/C$  possessed a onset potential of  $\sim 0.91 \text{ V vs. RHE}$  [34]. Recently, Liu et. al. prepared a freestanding Pd–Ru distorted icosahedral cluster as a HER catalyst, and the operating  $\eta$  value is 26 mV at a current density of  $10 \text{ mA cm}^{-2}$  [35]. Despite great progress,

there are still several issues that remain to be resolved. Specifically, the activity and stability of the above catalysts are still not that desirable, and the metal percentage of these catalysts was also very high, hence the catalysts are not cost-effective. More importantly, all of the above catalysts possessed either an ORR or HER functionality. To that end, designing Pd–Ru alloyed nanoparticles based electrocatalysts with high-efficiency, robust stability, and dual functionalities toward both ORR and HER is still imperative.

On the basis of our previous work of preparing porous carbon nanosheets (CNs) from metal–organic frameworks [36,37], herein, to the best of our knowledge, the Pd–Ru alloyed nanoparticles encapsulated in porous carbon nanosheets derived from MOFs were first fabricated and employed as a bifunctional electrocatalyst for both ORR and HER. By changing the variation of the Pd-to-Ru ratio, the composition and structure of the as-formed catalysts were fine-tuned. The Pd<sup>2+</sup> and Ru<sup>3+</sup> ions were adsorbed onto/into the carbon nanosheets, and in-situ reduced by a NaBH<sub>4</sub> aqueous solution. The hybrid nanocomposites were characterized by TEM, SEM, XRD, and XPS. The hybrids exhibited effective ORR and HER activity. Among the series of samples, Pd<sub>50</sub>Ru<sub>50</sub>/CNs stood out as the best catalyst for both ORR and HER, and its ORR performance was comparable to that of commercial Pd/C, while the HER activity was superior to the Pd/C in both acid and alkaline solutions. Notably, Pd<sub>50</sub>Ru<sub>50</sub>/CNs also exhibited remarkably outperformed long-term stability than the commercial Pd/C in both reactions. The novelty and significance of this work lie in several aspects. First of all, the Pd–Ru alloys encapsulated in carbon nanosheets derived from metal organic frameworks were first fabricated with dual catalytic functionalities toward both ORR and HER. Secondly, the Pd–Ru alloying effects plus the synergistic effects between the alloys and the carbon support significantly enhanced the electrocatalytic activity. Finally, the sample preparation method is quite facile and straightforward, in addition to the very low metal loading in the sample, which made the sample very cost effective resulting in potential practical application values.

## 2. Results and Discussions

### 2.1. Morphological Characterization

The porous carbon nanosheets were first prepared and examined by scanning electron microscope (SEM). The typical scanning electron microscopic (SEM) and transmission electron microscopic (TEM) images of carbon nanosheets can be found in Figure S1a,b. In Figure S1a,b, one may notice that carbon nanosheets with well-defined mesopores were obtained. The detailed microstructure of the Pd<sub>50</sub>Ru<sub>50</sub>/CNs sample was then characterized by TEM, high resolution transmission electron microscope (HR-TEM), and energy dispersive X-ray spectroscopic (EDS) mapping (Figure 1). It can be noted that the nanoparticles are highly crystalline and, based on more than 100 individual particles, the average diameter of the Pd–Ru nanoparticles was calculated as  $3.67 \pm 0.96$  nm (Inset in Figure 1a). As shown in Figure 1b, the lattice spacing of Pd<sub>50</sub>Ru<sub>50</sub>/CNs was identified as 0.194 nm for Pd (200), which is slightly smaller than that of pure Pd (0.1954 nm, JCPDS no. 87–0643). The slight decrease indicates the formation of the Pd–Ru alloy in Pd<sub>50</sub>Ru<sub>50</sub>/CNs [38,39]. The EDS elemental mapping of Pd<sub>50</sub>Ru<sub>50</sub>/CNs (Figure 1d–f) shows that the Pd and Ru elements are homogeneously dispersed in the sample with random inter-mixing, as evidenced by the overlapping pattern of Pd and Ru in Figure 1f. Such a phenomenon strongly indicates that a homogeneous Pd–Ru alloyed catalyst was obtained.

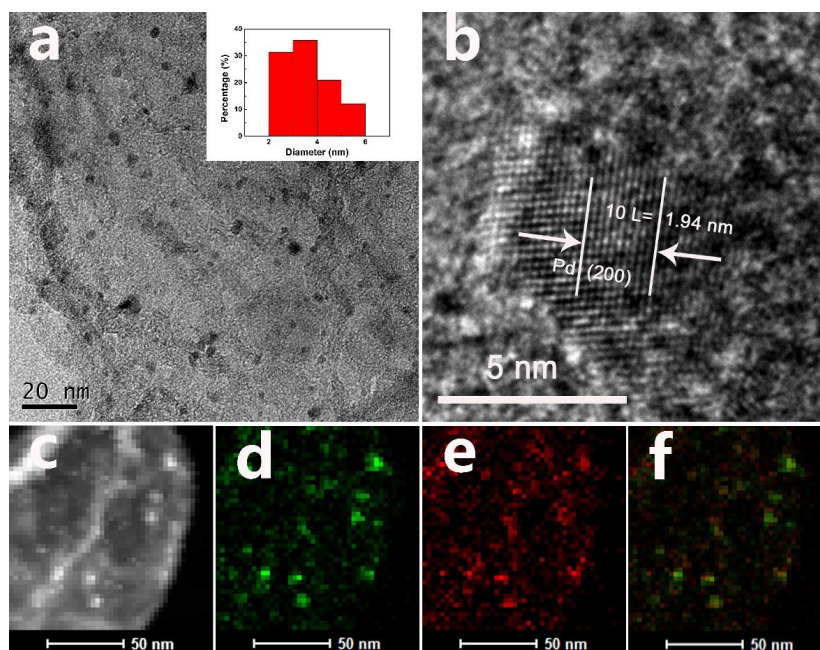


**Figure 1.** Representative (a) TEM image (inset is the size distribution histogram) and (b) high resolution (HR-TEM) image of Pd<sub>50</sub>Ru<sub>50</sub>/CNs. (c) Black field-TEM image of Pd<sub>50</sub>Ru<sub>50</sub>/CNs and energy dispersive X-ray spectroscopic (EDS) elemental mapping of (d) Pd, (e) Ru, and (f) Pd plus Ru elements in the Pd<sub>50</sub>Ru<sub>50</sub>/CNs.

The typical high-angle annular dark field-scanning tunneling electron microscopy (HAADF-STEM) and scanning electron microscopy (SEM) images of Pd<sub>50</sub>Ru<sub>50</sub>/CNs are displayed in Figure S2, and apparently, the Pd–Ru nanoparticles are well-dispersed onto/into the carbon nanosheets. In addition, the representative TEM images of the Pd<sub>33</sub>Ru<sub>67</sub>/CNs, Pd<sub>67</sub>Ru<sub>33</sub>/CNs, Pd<sub>100</sub>/CNs, and Ru<sub>100</sub>/CNs samples can be found in Figure S3. It can be noted that the Pd–Ru alloyed nanoparticles were all well dispersed on the carbon nanosheets, and very few aggregates can be observed. The average diameter was then analyzed as  $1.94 \pm 0.40$  nm,  $5.90 \pm 1.02$  nm,  $3.76 \pm 0.99$  nm, and  $1.55 \pm 0.57$  nm for Pd<sub>33</sub>Ru<sub>67</sub>/CNs, Pd<sub>67</sub>Ru<sub>33</sub>/CNs, Pd<sub>100</sub>/CNs, and Ru<sub>100</sub>/CNs, respectively, which is summarized in Table S1 as well.

To check whether the Pd–Ru nanoparticles are onto the surface or encapsulated into the pores of the carbon nanosheets, the Brunauer Emmet Teller (BET) measurement was then conducted. The BET surface areas and pore size distribution of the CNs and Pd<sub>50</sub>Ru<sub>50</sub>/CNs are depicted in Figure S4. The calculated BET surface area was  $1344.942 \text{ m}^2 \text{ g}^{-1}$  and  $489.565 \text{ m}^2 \text{ g}^{-1}$  for CNs and Pd<sub>50</sub>Ru<sub>50</sub>/CNs, respectively. Furthermore, the corresponding pore volumes for the two samples were  $1.576 \text{ cm}^3 \text{ g}^{-1}$  and  $0.76 \text{ cm}^3 \text{ g}^{-1}$ . The significant decrease of the BET surface area and pore volume after the addition of Pd and Ru strongly confirms that the Pd–Ru nanoparticles were indeed encapsulated in the pores of CNs.

## 2.2. X-ray Diffraction (XRD) and XPS Analysis

Figure 2a presents the XRD patterns of the Ru<sub>100</sub>/CNs, Pd<sub>50</sub>Ru<sub>50</sub>/CNs, and Pd<sub>100</sub>/CNs samples. The diffraction peak of Pd<sub>50</sub>Ru<sub>50</sub>/CNs at a  $2\theta$  value of  $39.94^\circ$ ,  $43.07^\circ$ ,  $46.19^\circ$ ,  $79.93^\circ$ , and  $80.82^\circ$  are in good accordance with the (111), (002), (200), (103), and (311) crystal planes of the face-centered cubic (fcc) alloyed structure, respectively. These peaks are located in the between of Ru<sub>100</sub>/CNs (JCPD-65-6490) [40] and Pd<sub>100</sub>/CNs (JCPD-87-0643) [41]. Furthermore, it can be seen from the inset enlarged view of Figure 2a, that after the addition of Ru, the diffraction peak of Pd<sub>50</sub>Ru<sub>50</sub>/CNs with  $2\theta$  at  $39.94^\circ$  showed a slightly positive shift about  $0.15^\circ$  compared to Pd<sub>100</sub>/CNs, which further confirmed the successful formation of Pd–Ru alloys. The XRD patterns of all of the samples are described in

Figure S5, and the  $2\theta$  value of diffraction peak at *ca.*  $40^\circ$  increases slightly with the increase of Ru in  $\text{Pd}_x\text{Ru}_{100-x}/\text{CNs}$ . The surface chemical composition and valence state of the as-prepared  $\text{Ru}_{100}/\text{CNs}$ ,  $\text{Pd}_{50}\text{Ru}_{50}/\text{CNs}$ , and  $\text{Pd}_{100}/\text{CNs}$  catalysts were then probed by XPS. Figure 2b presents the survey scan spectra of the  $\text{Pd}_{50}\text{Ru}_{50}/\text{CNs}$ ,  $\text{Pd}_{100}/\text{CNs}$ , and  $\text{Ru}_{100}/\text{CNs}$ . The discernible signal from Pd3d, Ru3d, and Ru3p electrons can be noted. Figure 2c presents the high-resolution spectra of the Pd3d electrons from both  $\text{Pd}_{50}\text{Ru}_{50}/\text{CNs}$  and  $\text{Pd}_{100}/\text{CNs}$ . For  $\text{Pd}_{50}\text{Ru}_{50}/\text{CNs}$ , the peak with a binding energy at 342.0 eV and 336.8 eV can be attributed to the Pd3d<sub>3/2</sub> and Pd3d<sub>5/2</sub> electrons, respectively [42]. The two peaks can be further deconvoluted into two pairs of doublets, and the peaks at the lower binding energies of 336.3 eV and 341.5 eV can be assigned to metallic Pd [36], while the peaks at higher binding energies of 337.6 eV and 343.1 eV are ascribed to the Pd (II) species [43,44]. This indicates the formation of palladium (II) oxides, which agree well with the Pd-carbon substrate hybrid systems in several previous reports [36,45,46]. Notably, compared with  $\text{Pd}_{100}/\text{CNs}$ , the binding energy for the Pd3d<sub>3/2</sub> electrons in  $\text{Pd}_{50}\text{Ru}_{50}/\text{CNs}$  shifted positively slightly, with a value of 0.3 eV. The high-resolution spectra of the Ru3d electrons from both  $\text{Pd}_{50}\text{Ru}_{50}/\text{CNs}$  and  $\text{Ru}_{100}/\text{CNs}$  are shown in Figure 2d. For both catalysts, the peaks with the binding energy at 281.0 and 284.8 eV agree well with the binding energy of the Ru3d<sub>5/2</sub> and Ru3d<sub>3/2</sub> electrons, respectively. Interestingly, such binding energy values agree well with metallic Ru, and there is barely a binding energy shift between  $\text{Pd}_{50}\text{Ru}_{50}/\text{CNs}$  and  $\text{Ru}_{100}/\text{CNs}$ . The positive binding energy shift of the Pd3d electrons in  $\text{Pd}_{50}\text{Ru}_{50}/\text{CNs}$  indicates that there is electron transfer occurring from the Pd atoms to the Ru atoms. Previous investigations have shown that such an electron transfer could facilitate the electrocatalytic reaction kinetics, and can therefore significantly enhance the catalytic activity [47–49]. The high-resolution XPS spectra of the Pd3d and Ru3d electrons of the other samples in the series are presented in Figure S6a,b, respectively. It can be noted that, with the decrease of the Pd ratio in the series, the binding energy of the Pd3d electrons gradually increased while the binding energy of the Ru3d electrons remained almost the same for all of the samples, further attesting that there is electron transfer occurring from the Pd atoms to the Ru atoms in the Pd–Ru alloys.

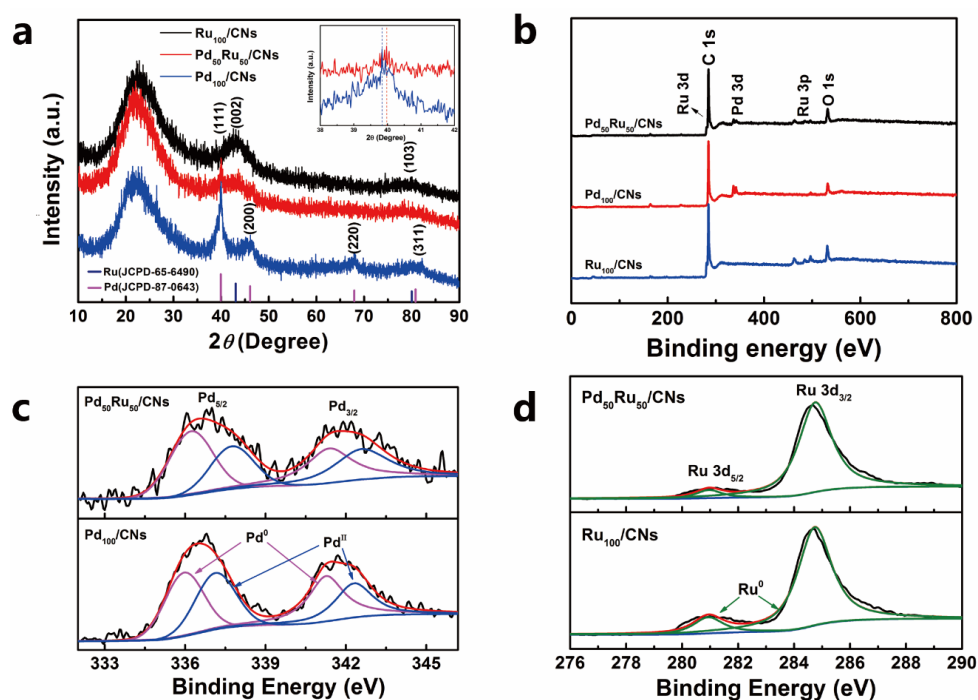


**Figure 2.** (a) The XRD patterns and (b) XPS survey scan spectra of the  $\text{Pd}_{50}\text{Ru}_{50}/\text{CNs}$ ,  $\text{Pd}_{100}/\text{CNs}$ , and  $\text{Ru}_{100}/\text{CNs}$ ; the core-level XPS spectra of (c) the Pd3d electrons for the  $\text{Pd}_{50}\text{Ru}_{50}/\text{CNs}$  and  $\text{Pd}_{100}/\text{CNs}$ ; and (d) the Ru3d electrons for the  $\text{Pd}_{50}\text{Ru}_{50}/\text{CNs}$  and  $\text{Ru}_{100}/\text{CNs}$ .

### 2.3. ORR Performance

The electrocatalytic performance of the series of samples toward ORR was first examined and summarized in Table S1. As illustrated in the cyclic voltammograms in Figure S7a, a peak at around 0.82 V vs. RHE attributable to oxygen reduction can be observed for all of the samples, suggesting the effective ORR activity. Figure S7b presents the RRDE (Rotating Ring Disk Electrode) curves of Ru<sub>100</sub>/CNs, Pd<sub>33</sub>Ru<sub>67</sub>/CNs, Pd<sub>50</sub>Ru<sub>50</sub>/CNs, Pd<sub>67</sub>Ru<sub>33</sub>/CNs, Pd<sub>100</sub>/CNs, and Pd/C in O<sub>2</sub>-saturated 0.1 M KOH solution, with a rotation rate of 1600 rpm. All of the samples demonstrated an excellent activity that is close to the commercial Pd/C, while Ru<sub>100</sub>/CNs exhibited a much lower activity. It is worth noting that the onset potential and diffusion-limited current density varied significantly with the change of Pd-to-Ru ratio. As compiled in Table S1, the onset potential first intensified then diminished with the decreasing of the Ru-to-Pd ratio. Pd<sub>50</sub>Ru<sub>50</sub>/CNs exhibited the best ORR performance with the most positive onset potential (0.903 V vs. RHE), and the largest diffusion-limited current density (5.14 mA cm<sup>-2</sup>) among the series. The onset potential is estimated as 0.841 V, 0.877 V, 0.895 V, and 0.877 V, and the diffusion-limited current density is approximately 3.27 mA cm<sup>-2</sup>, 4.26 mA cm<sup>-2</sup>, 3.99 mA cm<sup>-2</sup>, and 3.43 mA cm<sup>-2</sup> for Ru<sub>100</sub>/CNs, Pd<sub>33</sub>Ru<sub>67</sub>/CNs, Pd<sub>67</sub>Ru<sub>33</sub>/CNs, and Pd<sub>100</sub>/CNs at +0.3 V vs. RHE, respectively.

As Pd<sub>50</sub>Ru<sub>50</sub>/CNs stood out with the best performance in the series, its ORR performance was further assessed and compared with Pd/C. As shown in the cyclic voltammograms of Pd<sub>50</sub>Ru<sub>50</sub>/CNs and commercial Pd/C in Figure 3a, in O<sub>2</sub>-saturated 0.1 M KOH, both samples exhibited a peak around 0.75–0.85 V, which can be attributable to oxygen reduction. Figure 3b further illustrates the linear sweep voltammograms of Pd<sub>50</sub>Ru<sub>50</sub>/CNs and commercial Pd/C at the rotation of 1600 rpm, from where the onset potential and the diffusion-limited current density at +0.3 V can be determined as 0.903 V and 5.14 mA cm<sup>-2</sup>, and 0.915 V and 3.67 mA cm<sup>-2</sup>, for Pd<sub>50</sub>Ru<sub>50</sub>/CNs and commercial Pd/C, respectively. The onset potential of Pd<sub>50</sub>Ru<sub>50</sub>/CNs is comparable with that of Pd/C while its diffusion-limited current density is much larger, suggesting an outperformance toward the ORR of Pd<sub>50</sub>Ru<sub>50</sub>/CNs.

Furthermore, the corresponding electron transfer number (*n*) and the yield of H<sub>2</sub>O<sub>2</sub> in the ORR process can be calculated by the following equations:

$$n = \frac{4I_d}{I_r/N + I_d}$$

$$H_2O_2\% = \frac{200I_r/N}{I_r/N + I_d}$$

where *I<sub>d</sub>* represents the disk current (mA cm<sup>-2</sup>), *I<sub>r</sub>* is the ring current (mA cm<sup>-2</sup>), and *n* is the RRDE collection efficiency (0.37). The calculated results are presented in Figure 3c, where the electron transfer number was 3.73 to 3.89 and 3.66 to 3.91 for Pd<sub>50</sub>Ru<sub>50</sub>/CNs and commercial Pd/C in the potential range from 0 V to +0.80 V, respectively. Note that the *n* values for both samples are close to 4, indicating that a direct four-electron transfer pathway was taken. Correspondingly, the H<sub>2</sub>O<sub>2</sub> yield was 6.75% to 13.75% and 4.67% to 17.65% for Pd<sub>50</sub>Ru<sub>50</sub>/CNs and Pd/C, respectively, both of which are below 18%, suggesting that very little byproduct was generated during the catalytic process. The high electron transfer number and low hydrogen peroxide yield attest that the catalyst can catalyze the oxygen reduction very efficiently. Subsequently, linear sweep voltammetry (LSV) was conducted in the potential range of −0.034 to 1.166 V vs. RHE, with a scan rate of 10 mV s<sup>-1</sup> at rotation rate from 400 to 2025 rpm. The LSV curves are shown in Figure 3d, and it can be noted that the diffusion-limited current density increased with the increase of the rotation rate. The corresponding Koutecky–Levich (K–L) plots of Pd<sub>50</sub>Ru<sub>50</sub>/CNs are displayed in Figure 3e while such K–L plots for the other samples in the series, as well as Pd/C, are presented in Figure S8. Note that a great linearity with a very consistent slope was observed for all of the samples, and Pd/C, illustrating a first reaction-kinetics was adopted with regard to the concentration of the dissolved oxygen in solution.

To further elucidate the reaction kinetics, the Tafel plots of the series of samples and Pd/C were extrapolated from the corresponding K–L plots, and are shown in Figure 3f. The Tafel slope was calculated as  $72.9 \text{ mV dec}^{-1}$ ,  $77.7 \text{ mV dec}^{-1}$ ,  $70.1 \text{ mV dec}^{-1}$ ,  $80.9 \text{ mV dec}^{-1}$ ,  $86.9 \text{ mV dec}^{-1}$ , and  $84.6 \text{ mV dec}^{-1}$  for Ru<sub>100</sub>/CNs, Pd<sub>33</sub>Ru<sub>67</sub>/CNs, Pd<sub>50</sub>Ru<sub>50</sub>/CNs, Pd<sub>67</sub>Ru<sub>33</sub>/CNs, Pd<sub>100</sub>/CNs, and Pd/C, respectively. Pd<sub>50</sub>Ru<sub>50</sub>/CNs exhibited the lowest Tafel slope in the series, further attesting the best ORR activity in the series. Also, such a value is much lower than that of Pd/C, indicative of much faster reaction kinetics. Furthermore, all of the slope values are quite close with Pd/C, implying that a similar reaction mechanism was adopted for all of the samples. Such close Tafel slope values with Pd/C suggest that the rate-dominant step is probably the first-electron transfer to oxygen molecule, while the following reduction and the breaking of the O–O bond are relatively fast [48–50]. The above findings further confirm that Pd<sub>50</sub>Ru<sub>50</sub>/CNs exhibited slightly superior ORR activity than that of commercial Pd/C.

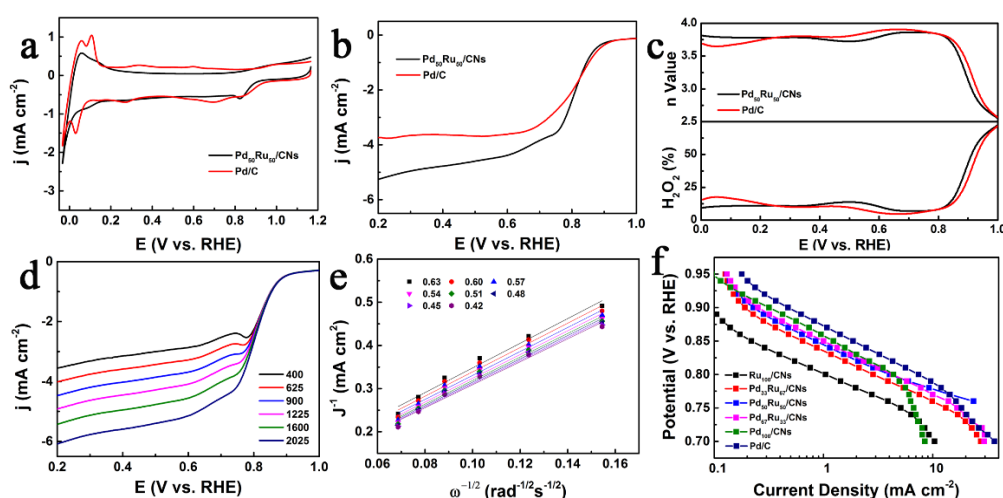


**Figure 3.** (a) Cyclic and (b) RRDE curves, (c) plots of H<sub>2</sub>O<sub>2</sub> yield, and electron transfer number of the Pd<sub>50</sub>Ru<sub>50</sub>/CNs and Pd/C catalysts. (d) linear sweep voltammograms (LSV) curves for Pd<sub>50</sub>Ru<sub>50</sub>/CNs at the rotation rates of 400–2025 rpm. (e) The Koutecky–Levich (K–L) plots for Pd<sub>50</sub>Ru<sub>50</sub>/CNs at various potentials. (f) Tafel plots of all of the samples and commercial 10 wt.% Pd/C. All of the measurements were performed in an oxygen-saturated 0.1 M KOH aqueous solution at a potential scan rate of  $10 \text{ mV s}^{-1}$ .

The durability of the Pd<sub>50</sub>Ru<sub>50</sub>/CNs sample was subsequently evaluated by chronoamperometric measurement at +0.5 V in 0.1 M KOH solution. As depicted in Figure 4a, after about 30,000 s, Pd/C retained 76.1% of its initial current, while in contrast, Pd<sub>50</sub>Ru<sub>50</sub>/CNs exhibited a loss of 11.4%, with 88.6% of its current preserved. It indicates that a higher long-term durability of Pd<sub>50</sub>Ru<sub>50</sub>/CNs than Pd/C was achieved. The tolerance against the methanol crossover is another important approach to evaluate the durability. Generally, because of the methanol crossover from anode to cathode, the equilibrium electrode potential will be blocked, and the catalyst is poisoned by the oxidation of these agents at the cathode, thus weakening the electrocatalytic activity in the fuel cell application [51]. Therefore, a cathode catalyst with selectivity is crucial in the presence of methanol species. Figure 4b shows the methanol sensitivity of the Pd<sub>50</sub>Ru<sub>50</sub>/CNs and Pd/C catalysts. The Pd/C catalyst exhibited a sudden decrease in the ORR current density when the methanol is injected, mainly due to the competitive reaction between ORR and methanol oxidation. However, upon the injection of methanol, Pd<sub>50</sub>Ru<sub>50</sub>/CNs showed a relatively smaller negative drop of the current density under the same conditions. These results imply that the Pd<sub>50</sub>Ru<sub>50</sub>/CNs possesses a more excellent methanol tolerance and selectivity toward ORR in presence of methanol than Pd/C. Such a finding also indicates that the

Pd<sub>50</sub>Ru<sub>50</sub>/CNs catalyst could serve as an efficient methanol tolerance catalyst and finds its applicability in methanol-based fuel cells as well.

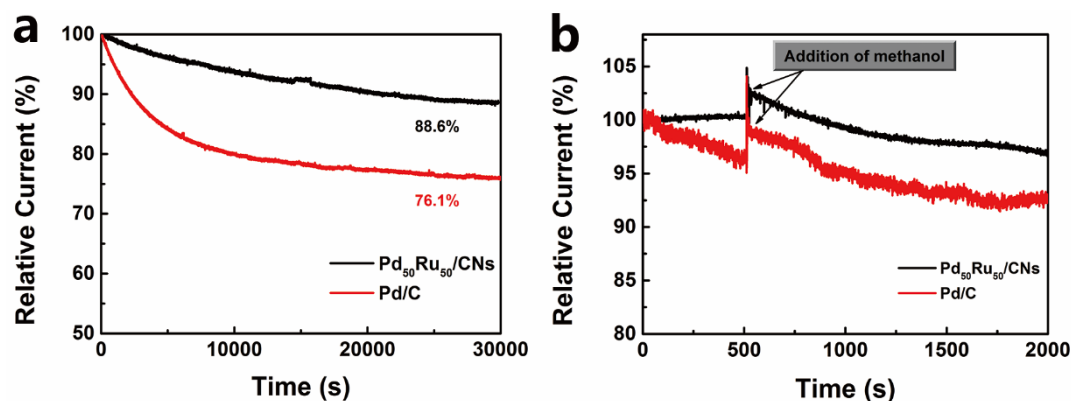


**Figure 4.** (a) Chronoamperometric curves of Pd<sub>50</sub>Ru<sub>50</sub>/CNs and Pd/C catalysts at +0.5 V for 30,000 s. (b) Chronoamperometric curves of Pd<sub>50</sub>Ru<sub>50</sub>/CNs and Pd/C at +0.5 V before and after the addition of methanol.

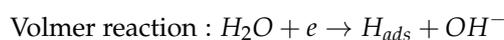
#### 2.4. HER Performance

Besides ORR, the HER performance of the series of samples was also assessed and compared with commercial Pd/C. Figure 5a presents the polarization curves of the series of samples and Pd/C. One can see that Pd<sub>100</sub>/CNs exhibited a very low activity, where effective activity was observed for the other samples and Pd/C as well. Notably, the HER activity intensified first then diminished with the increasing of the Pd percentage in the sample. At 10 mA cm<sup>-2</sup>, the overpotential was 63.7 mV for Ru<sub>100</sub>/CNs, 51.9 mV for Pd<sub>33</sub>Ru<sub>67</sub>/CNs, 37.3 mV for Pd<sub>50</sub>Ru<sub>50</sub>/CNs, 55.3 mV for Pd<sub>67</sub>Ru<sub>33</sub>/CNs, 254.4 mV for Pd<sub>100</sub>/CNs, and 77.2 mV for Pd/C, respectively. The sample of Pd<sub>50</sub>Ru<sub>50</sub>/CNs displayed the best HER activity, evidenced by the nearly zero onset potential and the lowest overpotential at 10 mA cm<sup>-2</sup>. Furthermore, the much lower overpotential at 10 mA cm<sup>-2</sup> from Pd<sub>50</sub>Ru<sub>50</sub>/CNs suggests that it had a more prominent HER outperformance than Pd/C. It is worth noting that there is a hydrogen adsorption peak around 0.4 V vs. RHE. The HER in the polarization curves of the Pd contained samples, which agrees well with several previous investigations regarding Pd-based nanomaterials for HER [44,52–54].

The Tafel equation plays a significant role in elucidating the kinetic mechanism of HER. The Tafel slope can be calculated by the following equation, derived from the polarization curves.

$$\eta = b \log j + a$$

where  $j$  is the measured current density (mA cm<sup>-2</sup>),  $b$  is the Tafel slope (mV dec<sup>-1</sup>), and  $a$  is an analyzed constant, respectively. The Tafel slope is calculated as 67.9 mV dec<sup>-1</sup> for Pd<sub>50</sub>Ru<sub>50</sub>/CNs, while a slope value of 109.9 mV dec<sup>-1</sup> was obtained for Pd/C (Figure 5b). The lower Tafel slope further confirms that the HER activity of Pd<sub>50</sub>Ru<sub>50</sub>/CNs is superior to Pd/C, as a small Tafel slope is desired to drive a large current density at a low overpotential [55]. The HER process in the alkaline electrolyte is generally considered as the Volmer–Heyrovsky process or the Volmer–Tafel pathway, as reported in previous studies [56,57], and they can be described as follows:



A Tafel slope of  $67.9 \text{ mV dec}^{-1}$  for Pd<sub>50</sub>Ru<sub>50</sub>/CNs indicates that the Volmer–Heyrosky mechanism is probably adopted [55,58].

The HER long-term stability of Pd<sub>50</sub>Ru<sub>50</sub>/CNs and Pd/C in a 0.1 M KOH solution were then probed and are illustrated in Figure 5c, d. By comparing the polarization curves of the two catalysts before and after potential scans, the cathodic current densities of the two catalysts decreased somewhat after the test. Pd<sub>50</sub>Ru<sub>50</sub>/CNs showed an 18.0 mV degradation at  $-20 \text{ mA cm}^{-2}$  after continuous potential scans of 1000 cycles, while Pd/C presented a negative shift of 51.8 mV at  $-20 \text{ mA cm}^{-2}$ . After 3000 cycles of potential scan, 33.8 mV and 82.2 mV of an overpotential negative shift were observed for Pd<sub>50</sub>Ru<sub>50</sub>/CNs and Pd/C, respectively. The much smaller potential decrease of Pd<sub>50</sub>Ru<sub>50</sub>/CNs suggests a remarkably superior stability in the alkaline media than Pd/C.

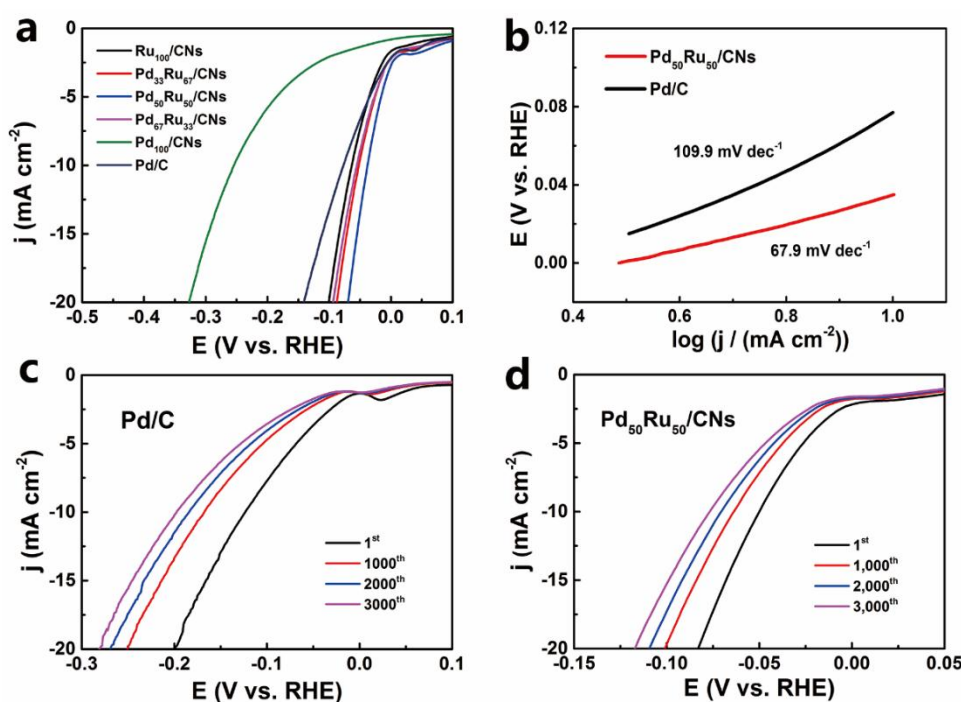


**Figure 5.** (a) The hydrogen evolution reaction (HER) polarization curves of the Pd<sub>100-x</sub>Ru<sub>x</sub>/CNs series and Pd/C in 0.1 M KOH. (b) The corresponding Tafel plots of the Pd<sub>50</sub>Ru<sub>50</sub>/CNs and Pd/C catalysts. Polarization curves after continuous potential scans of (c) Pd/C and (d) the Pd<sub>50</sub>Ru<sub>50</sub>/CNs at  $100 \text{ mV s}^{-1}$  in 0.1 M KOH.

In addition to alkaline media, the electrochemical HER activities of the series of samples and commercial Pd/C were also evaluated in a 0.5 M H<sub>2</sub>SO<sub>4</sub> solution by a standard three-electrode system. The polarization curves can be found in Figure S9a. The required HER overpotential to reach a current density of  $10 \text{ mA cm}^{-2}$  was 166.0 mV for Ru<sub>100</sub>/CNs, 76.0 mV for Pd<sub>33</sub>Ru<sub>67</sub>/CNs, 45.1 mV for Pd<sub>50</sub>Ru<sub>50</sub>/CNs, 60.5 mV for Pd<sub>67</sub>Ru<sub>33</sub>/CNs, 61.9 mV for Pd<sub>100</sub>/CNs, and 52.1 mV for Pd/C, respectively. The HER activity first increased and then decreased with the increasing of the Pd percentage, the same as the trend in the alkaline solution. Again, Pd<sub>50</sub>Ru<sub>50</sub>/CNs exhibited the best HER activity among the series in acid media. The corresponding Tafel slope was then calculated as  $67.6 \text{ mV dec}^{-1}$  and  $70.8 \text{ mV dec}^{-1}$  for Pd<sub>50</sub>Ru<sub>50</sub>/CNs and Pd/C (Figure S9b), implying that Pd<sub>50</sub>Ru<sub>50</sub>/CNs held a faster reaction kinetics than commercial Pd/C in acid electrolyte as well. Furthermore, the HER stability tests of Pd<sub>50</sub>Ru<sub>50</sub>/CNs and Pd/C in 0.5 M H<sub>2</sub>SO<sub>4</sub> were then conducted and displayed in Figure S9c,d. The cathodic current densities of both of the samples decreased upon the potential scans. After 1000 cycles, the required overpotential increased 29.5 mV and 25.6 mV for Pd/C and Pd<sub>50</sub>Ru<sub>50</sub>/CNs to drive a current density of  $40 \text{ mA cm}^{-2}$ , whereas after 3000 cycles, the increased overpotential was 78.8 mV and 58.0 mV for Pd/C and Pd<sub>50</sub>Ru<sub>50</sub>/CNs, respectively.

The results solidly attest that Pd<sub>50</sub>Ru<sub>50</sub>/CNs possessed a much higher long-term stability than Pd/C for HER in acid media as well.

It is worth noting that Pd<sub>50</sub>Ru<sub>50</sub>/CNs exhibited the best ORR and HER activities among the series. This is probably accounted for the maximal alloying effects in this sample. Take ORR as an example, as Pd and Ru have a different bonding interaction with oxygenated species, the Pd-to-Ru ratio of 1: 1 probably represents the optimal balance. Moreover, alloying with a second metal may lead to third body effect [59]. The close and proximal contact of Pd and Ru with molar ratio of 1: 1 might maximize the third body effect and increase the active sites on the nanoparticle's surface, and thus Pd<sub>50</sub>Ru<sub>50</sub>/CNs displayed the most outstanding catalytic performance [60].

The excellent ORR and HER activities and enhanced long-term stability of Pd<sub>50</sub>Ru<sub>50</sub>/CNs can be accounted to several factors. First of all, a significant contribution can be attributed to the Pd alloying Ru induced synergistic effects. Previous studies have shown that the introduction of a second metal component can significantly modify the surface geometric and electronic structure of the metal architectures, hence dramatically improve the catalytic activity and stability of the alloys [13,61]. Secondly, the porous carbon nanosheets (CNs) not only have a high electrical conductivity, but also offer additional active sites for the electrocatalytic process [62,63]. Meanwhile, the well-defined pore structure of the CNs can not only prevent the aggregation, decomposition, and coalescence of Pd–Ru alloyed nanoparticles, but also offer electron transfer and mass transport pathway for electrocatalytic reactions [37,64]; Finally, the interaction between the Pd–Ru nanoparticles and CNs might be favorable for the integrity of the composite and enhancing the electrocatalytic activity [17].

### 3. Materials and Methods

#### 3.1. Chemicals

The following reagents were all used as received without further purification: Zinc nitrate hexahydrate (Zn(NO<sub>3</sub>)<sub>2</sub>·6H<sub>2</sub>O, 99%, Fuchen Reagents, Tianjin, China), Terephthalic acid (H<sub>2</sub>BDC, 99%, Energy Chemicals, Shanghai, China), Sodium tetra-chloropalladate (Na<sub>2</sub>PdCl<sub>4</sub>, 99.95%, Energy Chemicals, Shanghai, China), Ruthenium(III) chloride (RuCl<sub>3</sub>, Energy Chemicals, Shanghai, China), Cetyltrimethylammonium bromide (CTAB, 99%, Fuchen Reagents, Tianjin, China). Triethylamine (TEA, 99%, Fuchen Reagents, Tianjin, China), Sodium borohydride (NaBH<sub>4</sub>, 98%, Aladdin Industrial Corporation, Shanghai, China), Commercial Pd/C (10%, Energy Chemicals, Shanghai, China), Hydrochloric acid (HCl, 36–38%, National Medicines Corporation Ltd, Beijing, China), Trichloromethane (CHCl<sub>3</sub>, Damao Chemical Reagents, Tianjin, China), and N, N-dimethylformamide (DMF, 99.5%, Fuchen Reagents, Tianjin, China). Distilled water (resistivity: 18.3 MΩ·cm) was employed in this study.

#### 3.2. Preparation of Porous Carbon Nanosheets (CNs)

The carbon nanosheets were fabricated by following a protocol documented in our previous work [17,36]. Typically, 30 mmol of Zn(NO<sub>3</sub>)<sub>2</sub>·6H<sub>2</sub>O and 10 mmol of terephthalic acid were co-dissolved in 250 mL of DMF by sonication, and was stirred for 3 h at room temperature. After being aged at 60 °C for 72 h in an oil bath, 50 mmol of CTAB were added, and the mixture was heated at 105 °C for another 90 min under magnetic stirring. Then, 6.95 mL TEA was injected immediately and the solution was stirred vigorously for 15 min. The precipitates formed and were collected by centrifugation when cooled down to room temperature, and washed by DMF and CHCl<sub>3</sub> three times, respectively. The obtained precipitates were then dried at 150 °C for 24 h in a vacuum oven. Subsequently, the nanocrystals acquired above were pyrolyzed at 900 °C in a quartz tube for 6 h with a heating rate of 5 °C min<sup>-1</sup> in a high pure N<sub>2</sub> atmosphere. After the furnace was cooled down to an ambient temperature, the black powder was collected and washed three times with diluted HCl to remove the impurities. The obtained solids were designated as CNs.

### 3.3. Preparation of Pd<sub>x</sub>Ru<sub>100-x</sub>/CNs

The Pd–Ru alloyed nanoparticles supported on carbon nanosheets (denoted as Pd<sub>x</sub>Ru<sub>100-x</sub>/CNs, where x presents the molar percentage of Pd in total metal) were prepared by a wet-chemical approach. For the synthesis of Pd<sub>50</sub>Ru<sub>50</sub>/CNs, the procedure is as follows: Briefly, 31.12 mg of the as-synthesized CNs were well-dispersed in 13 mL of deionized water by sonication for 15 min and stirring for 15 min, respectively. Subsequently, 4.90 mg of Na<sub>2</sub>PdCl<sub>4</sub> dissolved in 1 mL H<sub>2</sub>O and 3.46 mg of RuCl<sub>3</sub> dissolved in 1 mL H<sub>2</sub>O were added and the mixture were stirred for 20 min, followed by the addition of 12.6 mg of a freshly-prepared NaBH<sub>4</sub> aqueous solution under vigorously stirring. After continuous agitation for 2 h, the products were collected by centrifuging at 10000 rpm for 10 min and dried in a 35 °C vacuum oven for 24 h. The total mass percentage of metal is set as 10%. Other samples were prepared in a similar manner, except for different molar ratios (1:0, 1:2, 2:1, 0:1) of ruthenium-to-palladium, which were denoted as Ru<sub>100</sub>/CNs, Pd<sub>33</sub>Ru<sub>67</sub>/CNs, Pd<sub>67</sub>Ru<sub>33</sub>/CNs, and Pd<sub>100</sub>/CNs, respectively.

### 3.4. Morphological Characterizations

The size and morphology of the as-formed Pd<sub>x</sub>Ru<sub>100-x</sub>/CNs were observed by a high-resolution transmission electron microscope (TEM) (JEOL TEM-2010, JEOL Ltd., Tokyo, Japan) along with an energy dispersive X-ray spectroscopy (EDS) system (Carl Zeiss AG, Jena, Germany). The crystal structures of the products were revealed by X-ray diffraction (XRD) (Bruker, NASDAQ, USA) using a Cu K<sub>α</sub> radiation ( $\lambda = 0.1541$  nm) equipped Bruker D8 diffractometer. The electronic structure of the nanoparticles was probed by X-ray photoelectron spectroscopy (XPS) (PHI X-tool, GaoDeYingTe Technology Co., Ltd., Hongkong, China) with a photoelectron spectrometer of Escalab 250 (Thermo Fisher Scientific, Waltham, MA, USA). The Brunauer Emmet Teller (BET) surface areas and pore size measurements were conducted on a Quantachrome Autosorb-iQ2 (Quantachrome, Boynton Beach, FL, USA) instrument with N<sub>2</sub> adsorption/adsorption isotherms at 77 K.

### 3.5. Electrochemical Measurements

All of the electrochemical measurements were operated on a CHI 750E electrochemical workstation (CH Instruments Inc.) at room temperature. The ORR measurements were carried out with a conventional three-electrode system, including a glassy carbon-disk electrode (diameter 5 mm, Pine Instrument Inc., RRDE collection efficiency is 37%) as the working electrode, an AgCl/Ag ( $E_{(RHE)} = E_{(Ag/AgCl)} + (0.197 + 0.0591 \text{ pH}) \text{ V}$ ) electrode as the reference electrode, and a platinum wire as the counter electrode in 0.1 M KOH aqueous solution. The glassy carbon disk was polished with aqueous slurries of 200 nm alumina powders prior to 20  $\mu\text{L}$  of 2 mg/mL of catalyst ink was dropwisely cast and air dried. Then, 10  $\mu\text{L}$  of diluted Nafion solution (20  $\mu\text{L}$  5 wt % Nafion in 980  $\mu\text{L}$  ethanol) was placed on the glassy carbon disk and dried in air. Prior to the ORR measurement, the electrolytes were saturated with O<sub>2</sub> by bubbling O<sub>2</sub> for at least 30 min. The cyclic voltammograms (CV) and linear sweep voltammograms (LSV) with rotation rate from 100 to 2500 rpm were recorded at a scan rate of 10 mV s<sup>-1</sup> in the potential range from -0.034 V to 1.166 V vs. RHE in oxygen-saturated 0.1 M KOH solution. The stability of the as-prepared catalyst and commercial Pd/C were examined by chronoamperometric measurements and methanol poisoning test at the potential of + 0.5 V with a rotation rate of 900 rpm.

The HER measurements were performed in both 0.5 M H<sub>2</sub>SO<sub>4</sub> and 0.1 M KOH electrolytes, with a scan rate of 10 mV s<sup>-1</sup> at room temperature. In both tests, a glassy carbon electrode (GCE, diameter 3 mm) and a graphite rod were employed as the working electrode and the counter electrode, respectively. The reference electrode employed was an AgCl/Ag electrode and a saturated calomel electrode (SCE) ( $E_{(RHE)} = E_{(SCE)} + (0.24 + 0.0591 \text{ pH}) \text{ V}$ ) in 0.1 M KOH and 0.5 M H<sub>2</sub>SO<sub>4</sub>, respectively. Then, 12.5  $\mu\text{L}$  of 2 mg/mL of catalyst ink and 10  $\mu\text{L}$  of diluted Nafion were dropwisely cast on the GCE successively. The durability of the Pd<sub>50</sub>Ru<sub>50</sub>/CNs catalyst and commercial Pd/C was

assessed by accelerated linear potential sweeps conducted repeatedly on the electrode at a scan rate of  $100 \text{ mV s}^{-1}$ .

#### 4. Conclusions

In conclusion, a series of Pd–Ru alloys encapsulated in porous carbon nanosheets were fabricated and employed as dual functional catalysts, both ORR and HER. All of the alloyed samples demonstrated effective catalytic activities toward both ORR and HER. Pd<sub>50</sub>Ru<sub>50</sub>/CNs showed the best bifunctional catalytic performance among the series, whose ORR activity is comparable to commercial Pd/C, while the HER activity is superior to Pd/C. Moreover, the Pd<sub>50</sub>Ru<sub>50</sub>/CNs sample demonstrated, markedly outperformed long-term stability than Pd/C for both ORR and HER. The strategy for encapsulating bimetallic alloys within porous carbon materials is promising for fabricating dual functional electrocatalysts with controllable composition and optimized activity for fuel cell applications and potential massive hydrogen generation.

**Supplementary Materials:** The following are available online at <http://www.mdpi.com/2073-4344/8/8/329/s1>, Figure S1: (a) The typical SEM and (b) TEM images of porous carbon nanosheets., Figure S2: (a) The typical high-angle annular dark field-scanning tunneling electron microscopy (HAADF-STEM) and (b) Scanning electron microscopy (SEM) images of Pd<sub>50</sub>Ru<sub>50</sub>/CNs., Figure S3: The representative TEM images of (a) Pd<sub>33</sub>Ru<sub>67</sub>/CNs ( $1.94 \pm 0.40 \text{ nm}$ ), (b) Pd<sub>67</sub>Ru<sub>33</sub>/CNs ( $5.90 \pm 1.02 \text{ nm}$ ), (c) Pd<sub>100</sub>/CNs ( $3.76 \pm 0.99 \text{ nm}$ ) and (d) Ru<sub>100</sub>/CNs ( $1.55 \pm 0.57 \text{ nm}$ ). (Inset is the corresponding size distribution histogram)., Figure S4: (a, c) Nitrogen adsorption/desorption isotherms at 77 K and (b, d) the corresponding pore-size distribution of CNs and Pd<sub>50</sub>Ru<sub>50</sub>/CNs., Figure S5: The XRD patterns of all the samples., Figure S6: The high-resolution XPS spectra of the (a) Pd3d and (b) Ru3d electrons in the series of samples., Figure S7: (a) The CV curves and (b) RRDE voltammograms of all the Pd<sub>x</sub>Ru<sub>100-x</sub>/CNs alloyed samples and Pd/C in O<sub>2</sub>-saturated 0.1 M KOH solution., Figure S8: The Koutecky-Levich (K-L) plots of (a) Ru<sub>100</sub>/CNs, (b) Pd<sub>33</sub>Ru<sub>67</sub>/CNs, (c) Pd<sub>67</sub>Ru<sub>33</sub>/CNs, (d) Pd<sub>100</sub>/CNs and (e) Pd/C., Figure S9: HER activity curves (a) of PdRu alloy CNs and Pd/C in 0.5 M H<sub>2</sub>SO<sub>4</sub> with scan rate of  $10 \text{ mV s}^{-1}$ . The corresponding Tafel plots (b) of the Pd<sub>50</sub>Ru<sub>50</sub>/CNs and Pd/C catalyst. Polarization curves after continuous potential sweeps of Pd/C (c) and Pd<sub>50</sub>Ru<sub>50</sub>/CNs (d) at  $100 \text{ mV s}^{-1}$  in 0.5 M H<sub>2</sub>SO<sub>4</sub>, Table S1: The summary of the ORR performance and size of the samples with different Pd-to-Ru ratios (The total metal mass loading was set as 10%).

**Author Contributions:** Conceptualization, Z.T.; Data curation, J.T. and W.W.; Formal analysis, Y.W. and S.C.; Funding acquisition, Z.T.; Investigation, J.T.; Project administration, Z.T.; Resources, Z.T.; Supervision, Z.T.; Writing—original draft, W.W.; Writing—review & editing, Z.T., R.B., B.T. and Z.L.

**Acknowledgments:** Zhenghua Tang thanks the financial support from the National Natural Science Foundation of China (21501059), the Guangdong Natural Science Funds for Distinguished Young Scholars (No. 2015A030306006), the Guangdong Innovative and Entrepreneurial Research Team Program (No. 2014ZT05N200), the Science and Technology Program of Guangdong Province (No. 2017A050506014), and the Guangzhou Science and Technology Plan Projects (No. 201804010323).

**Conflicts of Interest:** The authors declare no conflict of interest.

#### References

1. Winter, M.; Brodd, R.J. What Are Batteries, Fuel Cells, and Supercapacitors? *Chem. Rev.* **2004**, *104*, 4245–4270. [[CrossRef](#)] [[PubMed](#)]
2. Liu, X.-W.; Li, W.-W.; Yu, H.-Q. Cathodic catalysts in bioelectrochemical systems for energy recovery from wastewater. *Chem. Soc. Rev.* **2014**, *43*, 7718–7745. [[CrossRef](#)] [[PubMed](#)]
3. Xu, Y.; Kraft, M.; Xu, R. Metal-free carbonaceous electrocatalysts and photocatalysts for water splitting. *Chem. Soc. Rev.* **2016**, *45*, 3039–3052. [[CrossRef](#)] [[PubMed](#)]
4. Li, Y.; Gong, M.; Liang, Y.; Feng, J.; Kim, J.-E.; Wang, H.; Hong, G.; Zhang, B.; Dai, H. Advanced zinc-air batteries based on high-performance hybrid electrocatalysts. *Nat. Commun.* **2013**, *4*, 1805. [[CrossRef](#)] [[PubMed](#)]
5. Liu, M.; Zhang, R.; Chen, W. Graphene-Supported Nanoelectrocatalysts for Fuel Cells: Synthesis, Properties, and Applications. *Chem. Rev.* **2014**, *114*, 5117–5160. [[CrossRef](#)] [[PubMed](#)]
6. Tang, Z.; Wu, W.; Wang, K. Oxygen Reduction Reaction Catalyzed by Noble Metal Clusters. *Catalysts* **2018**, *8*, 65. [[CrossRef](#)]

7. Wang, J.; Xu, F.; Jin, H.; Chen, Y.; Wang, Y. Non-Noble Metal-based Carbon Composites in Hydrogen Evolution Reaction: Fundamentals to Applications. *Adv. Mater.* **2017**, *29*, 1605838. [[CrossRef](#)] [[PubMed](#)]
8. Wang, L.; Tang, Z.; Yan, W.; Wang, Q.; Yang, H.; Chen, S. Co@Pt Core@Shell nanoparticles encapsulated in porous carbon derived from zeolitic imidazolate framework 67 for oxygen electroreduction in alkaline media. *J. Power Sources* **2017**, *343*, 458–466. [[CrossRef](#)]
9. Shao, M.; Chang, Q.; Dodelet, J.-P.; Chenitz, R. Recent Advances in Electrocatalysts for Oxygen Reduction Reaction. *Chem. Rev.* **2016**, *116*, 3594–3657. [[CrossRef](#)] [[PubMed](#)]
10. Wang, M.; Chen, L.; Sun, L. Recent progress in electrochemical hydrogen production with earth-abundant metal complexes as catalysts. *Energy Environ. Sci.* **2012**, *5*, 6763–6778. [[CrossRef](#)]
11. Antolini, E. Palladium in fuel cell catalysis. *Energy Environ. Sci.* **2009**, *2*, 915–931. [[CrossRef](#)]
12. Jiang, H.-L.; Xu, Q. Recent progress in synergistic catalysis over heterometallic nanoparticles. *J. Mater. Chem.* **2011**, *21*, 13705–13725. [[CrossRef](#)]
13. Gilroy, K.D.; Ruditskiy, A.; Peng, H.-C.; Qin, D.; Xia, Y. Bimetallic Nanocrystals: Syntheses, Properties, and Applications. *Chem. Rev.* **2016**, *116*, 10414–10472. [[CrossRef](#)] [[PubMed](#)]
14. Gao, F.; Goodman, D.W. Pd-Au bimetallic catalysts: Understanding alloy effects from planar models and (supported) nanoparticles. *Chem. Soc. Rev.* **2012**, *41*, 8009–8020. [[CrossRef](#)] [[PubMed](#)]
15. Tao, F. Synthesis, catalysis, surface chemistry and structure of bimetallic nanocatalysts. *Chem. Soc. Rev.* **2012**, *41*, 7977–7979. [[CrossRef](#)] [[PubMed](#)]
16. He, L.-L.; Song, P.; Wang, A.-J.; Zheng, J.-N.; Mei, L.-P.; Feng, J.-J. A general strategy for the facile synthesis of AuM (M = Pt/Pd) alloyed flowerlike-assembly nanochains for enhanced oxygen reduction reaction. *J. Mater. Chem. A* **2015**, *3*, 5352–5359. [[CrossRef](#)]
17. Yan, W.; Tang, Z.; Wang, L.; Wang, Q.; Yang, H.; Chen, S. PdAu alloyed clusters supported by carbon nanosheets as efficient electrocatalysts for oxygen reduction. *Int. J. Hydrogen Energy* **2017**, *42*, 218–227. [[CrossRef](#)]
18. Li, S.-S.; Wang, A.-J.; Hu, Y.-Y.; Fang, K.-M.; Chen, J.-R.; Feng, J.-J. One-step, seedless wet-chemical synthesis of gold@palladium nanoflowers supported on reduced graphene oxide with enhanced electrocatalytic properties. *J. Mater. Chem. A* **2014**, *2*, 18177–18183. [[CrossRef](#)]
19. Chen, C.-W.; Hsieh, Y.-S.; Syu, C.-C.; Chen, H.-R.; Lee, C.-L. Displacement preparation-induced effects on structure of Ag–Pd nanobrushes for catalyzing oxygen reduction. *J. Alloy. Compd.* **2013**, *580*, S359–S363. [[CrossRef](#)]
20. Sekol, R.C.; Li, X.; Cohen, P.; Doubek, G.; Carmo, M.; Taylor, A.D. Silver palladium core–shell electrocatalyst supported on MWNTs for ORR in alkaline media. *Appl. Catal. B: Environ.* **2013**, *138–139*, 285–293. [[CrossRef](#)]
21. Xu, L.; Luo, Z.; Fan, Z.; Zhang, X.; Tan, C.; Li, H.; Zhang, H.; Xue, C. Triangular Ag-Pd alloy nanoprisms: Rational synthesis with high-efficiency for electrocatalytic oxygen reduction. *Nanoscale* **2014**, *6*, 11738–11743. [[CrossRef](#)] [[PubMed](#)]
22. Qi, Y.; Wu, J.; Zhang, H.; Jiang, Y.; Jin, C.; Fu, M.; Yang, H.; Yang, D. Facile synthesis of Rh-Pd alloy nanodendrites as highly active and durable electrocatalysts for oxygen reduction reaction. *Nanoscale* **2014**, *6*, 7012–7018. [[CrossRef](#)] [[PubMed](#)]
23. Li, B.; Prakash, J. Oxygen reduction reaction on carbon supported Palladium–Nickel alloys in alkaline media. *Electrochem. Commun.* **2009**, *11*, 1162–1165. [[CrossRef](#)]
24. Liu, S.; Zhang, Q.; Li, Y.; Han, M.; Gu, L.; Nan, C.; Bao, J.; Dai, Z. Five-Fold Twinned Pd<sub>2</sub>NiAg Nanocrystals with Increased Surface Ni Site Availability to Improve Oxygen Reduction Activity. *J. Am. Chem. Soc.* **2015**, *137*, 2820–2823. [[CrossRef](#)] [[PubMed](#)]
25. Yun, M.; Ahmed, M.S.; Jeon, S. Thiolated graphene oxide-supported palladium cobalt alloyed nanoparticles as high performance electrocatalyst for oxygen reduction reaction. *J. Power Sources* **2015**, *293*, 380–387. [[CrossRef](#)]
26. Kuttiyiel, K.A.; Sasaki, K.; Su, D.; Wu, L.J.; Zhu, Y.M.; Adzic, R.R. Gold-promoted structurally ordered intermetallic palladium cobalt nanoparticles for the oxygen reduction reaction. *Nat. Commun.* **2014**, *5*, 5185. [[CrossRef](#)] [[PubMed](#)]
27. Zheng, Y.; Zhao, S.; Liu, S.; Yin, H.; Chen, Y.-Y.; Bao, J.; Han, M.; Dai, Z. Component-Controlled Synthesis and Assembly of Cu–Pd Nanocrystals on Graphene for Oxygen Reduction Reaction. *ACS Appl. Mater. Interfaces* **2015**, *7*, 5347–5357. [[CrossRef](#)] [[PubMed](#)]

28. Kim, J.; Park, J.-E.; Momma, T.; Osaka, T. Synthesis of Pd–Sn nanoparticles by ultrasonic irradiation and their electrocatalytic activity for oxygen reduction. *Electrochim. Acta* **2009**, *54*, 3412–3418. [[CrossRef](#)]
29. Hubkowska, K.; Łukaszewski, M.; Czerwiński, A. Pd–Ru electrodeposits with high hydrogen absorption capacity. *Electrochem. Commun.* **2012**, *20*, 175–177. [[CrossRef](#)]
30. Peng, Y.; Lu, B.; Chen, L.; Wang, N.; Lu, J.E.; Ping, Y.; Chen, S. Hydrogen evolution reaction catalyzed by ruthenium ion-complexed graphitic carbon nitride nanosheets. *J. Mater. Chem. A* **2017**, *5*, 18261–18269. [[CrossRef](#)]
31. Zhang, J.; Liu, P.; Wang, G.; Zhang, P.P.; Zhuang, X.D.; Chen, M.W.; Weidinger, I.M.; Feng, X.L. Ruthenium/nitrogen-doped carbon as an electrocatalyst for efficient hydrogen evolution in alkaline solution. *J. Mater. Chem. A* **2017**, *5*, 25314–25318. [[CrossRef](#)]
32. Zheng, Y.; Jiao, Y.; Zhu, Y.; Li, L.H.; Han, Y.; Chen, Y.; Jaroniec, M.; Qiao, S.-Z. High Electrocatalytic Hydrogen Evolution Activity of an Anomalous Ruthenium Catalyst. *J. Am. Chem. Soc.* **2016**, *138*, 16174–16181. [[CrossRef](#)] [[PubMed](#)]
33. Shao, M.H.; Huang, T.; Liu, P.; Zhang, J.; Sasaki, K.; Vukmirovic, M.B.; Adzic, R.R. Palladium Monolayer and Palladium Alloy Electrocatalysts for Oxygen Reduction. *Langmuir* **2006**, *22*, 10409–10415. [[CrossRef](#)] [[PubMed](#)]
34. Sun, Y.; Hsieh, Y.-C.; Chang, L.-C.; Wu, P.-W.; Lee, J.-F. Synthesis of Pd<sub>9</sub>Ru@Pt nanoparticles for oxygen reduction reaction in acidic electrolytes. *J. Power Sources* **2015**, *277*, 116–123. [[CrossRef](#)]
35. Liu, S.; Zhang, Q.; Bao, J.; Li, Y.; Dai, Z.; Gu, L. Significantly Enhanced Hydrogen Evolution Activity of Freestanding Pd–Ru Distorted Icosahedral Clusters with less than 600 Atoms. *Chem. Eur. J.* **2017**, *23*, 18203–18207. [[CrossRef](#)] [[PubMed](#)]
36. Yan, W.; Tang, Z.; Li, L.; Wang, L.; Yang, H.; Wang, Q.; Wu, W.; Chen, S. Ultrasmall Palladium Nanoclusters Encapsulated in Porous Carbon Nanosheets for Oxygen Electroreduction in Alkaline Media. *ChemElectroChem* **2017**, *4*, 1349–1355. [[CrossRef](#)]
37. Wang, Q.; Wang, L.; Tang, Z.; Wang, F.; Yan, W.; Yang, H.; Zhou, W.; Li, L.; Kang, X.; Chen, S. Oxygen reduction catalyzed by gold nanoclusters supported on carbon nanosheets. *Nanoscale* **2016**, *8*, 6629–6635. [[CrossRef](#)] [[PubMed](#)]
38. Bin, D.; Yang, B.; Ren, F.; Zhang, K.; Yang, P.; Du, Y. Facile synthesis of PdNi nanowire networks supported on reduced graphene oxide with enhanced catalytic performance for formic acid oxidation. *J. Mater. Chem. A* **2015**, *3*, 14001–14006. [[CrossRef](#)]
39. Xiong, Z.; Xu, H.; Li, S.; Gu, Z.; Yan, B.; Guo, J.; Du, Y. Concave Pd–Ru nanocubes bounded with high active area for boosting ethylene glycol electrooxidation. *Appl. Surf. Sci.* **2018**, *427*, 83–89. [[CrossRef](#)]
40. Lange, F.; Armbruster, U.; Martin, A. Heterogeneously-Catalyzed Hydrogenation of Carbon Dioxide to Methane using RuNi Bimetallic Catalysts. *Energy Technol.* **2015**, *3*, 55–62. [[CrossRef](#)]
41. Meku, E.; Du, C.; Wang, Y.; Du, L.; Sun, Y.; Kong, F.; Yin, G. Concentration Gradient Pd–Ir–Ni/C Electrocatalyst with Enhanced Activity and Methanol Tolerance for Oxygen Reduction Reaction in Acidic Medium. *Electrochim. Acta* **2016**, *192*, 177–187. [[CrossRef](#)]
42. Wagner, C.D.; Riggs, W.M.; Davis, L.E.; Moulder, J.F.; Muilenberg, G.E. *Handbook of X-ray Photoelectron Spectroscopy: A Reference Book of Standard Data for Use in X-ray Photoelectron Spectroscopy*; Perkin-Elmer Corp., Physical Electronics Division: Eden Prairie, MN, USA, 1979; pp. 1–100.
43. Li, D.; Tang, Z.; Chen, S.; Tian, Y.; Wang, X. Peptide-FlgA<sub>3</sub>-Based Gold Palladium Bimetallic Nanoparticles That Catalyze the Oxygen Reduction Reaction in Alkaline Solution. *ChemCatChem* **2017**, *9*, 2980–2987. [[CrossRef](#)]
44. Li, T.; Tang, Z.; Wang, K.; Wu, W.; Chen, S.; Wang, C. Palladium nanoparticles grown on β-Mo<sub>2</sub>C nanotubes as dual functional electrocatalysts for both oxygen reduction reaction and hydrogen evolution reaction. *Int. J. Hydrogen Energy* **2018**, *43*, 4932–4941. [[CrossRef](#)]
45. Deming, C.P.; Mercado, R.; Gadiraju, V.; Sweeney, S.W.; Khan, M.; Chen, S. Graphene Quantum Dots-Supported Palladium Nanoparticles for Efficient Electrocatalytic Reduction of Oxygen in Alkaline Media. *ACS Sustainable Chem. Eng.* **2015**, *3*, 3315–3323. [[CrossRef](#)]
46. Deming, C.P.; Mercado, R.; Lu, J.E.; Gadiraju, V.; Khan, M.; Chen, S. Oxygen Electroreduction Catalyzed by Palladium Nanoparticles Supported on Nitrogen-Doped Graphene Quantum Dots: Impacts of Nitrogen Dopants. *ACS Sustainable Chem. Eng.* **2016**, *4*, 6580–6589. [[CrossRef](#)]

47. Du, C.; Gao, X.; Zhuang, Z.; Cheng, C.; Zheng, F.; Li, X.; Chen, W. Epitaxial growth of zigzag PtAu alloy surface on Au nano-pentagrams with enhanced Pt utilization and electrocatalytic performance toward ethanol oxidation reaction. *Electrochim. Acta* **2017**, *238*, 263–268. [[CrossRef](#)]
48. Zong, Z.; Xu, K.; Li, D.; Tang, Z.; He, W.; Liu, Z.; Wang, X.; Tian, Y. Peptide templated Au@Pd core-shell structures as efficient bi-functional electrocatalysts for both oxygen reduction and hydrogen evolution reactions. *J. Catal.* **2018**, *361*, 168–176. [[CrossRef](#)]
49. Wu, W.; Tang, Z.; Wang, K.; Liu, Z.; Li, L.; Chen, S. Peptide templated AuPt alloyed nanoparticles as highly efficient bi-functional electrocatalysts for both oxygen reduction reaction and hydrogen evolution reaction. *Electrochim. Acta* **2018**, *260*, 168–176. [[CrossRef](#)]
50. Wang, H.; Yang, N.; Li, W.; Ding, W.; Chen, K.; Li, J.; Li, L.; Wang, J.; Jiang, J.; Jia, F.; Wei, Z. Understanding the Roles of Nitrogen Configurations in Hydrogen Evolution: Trace Atomic Cobalt Boosts the Activity of Planar Nitrogen-Doped Graphene. *ACS Energy Lett.* **2018**, *3*, 1345–1352. [[CrossRef](#)]
51. Jahan, M.; Bao, Q.; Loh, K.P. Electrocatalytically Active Graphene–Porphyrin MOF Composite for Oxygen Reduction Reaction. *J. Am. Chem. Soc.* **2012**, *134*, 6707–6713. [[CrossRef](#)] [[PubMed](#)]
52. Łukaszewski, M.; Klimek, K.; Żurowski, A.; Kędra, T.; Czerwiński, A. Kinetics and mechanism of hydrogen electrosorption in palladium-based alloys. *Solid State Ionics* **2011**, *190*, 18–24. [[CrossRef](#)]
53. Safavi, A.; Kazemi, S.H.; Kazemi, H. Electrocatalytic behaviors of silver–palladium nanoalloys modified carbon ionic liquid electrode towards hydrogen evolution reaction. *Fuel* **2014**, *118*, 156–162. [[CrossRef](#)]
54. Ghasemi, S.; Hosseini, S.R.; Nabipour, S.; Asen, P. Palladium nanoparticles supported on graphene as an efficient electrocatalyst for hydrogen evolution reaction. *Int. J. Hydrogen Energy* **2015**, *40*, 16184–16191. [[CrossRef](#)]
55. Kong, D.; Cha, J.J.; Wang, H.; Lee, H.R.; Cui, Y. First-row transition metal dichalcogenide catalysts for hydrogen evolution reaction. *Energy Environ. Sci.* **2013**, *6*, 3553–3558. [[CrossRef](#)]
56. Yin, X.; Sun, G.; Wang, L.; Bai, L.; Su, L.; Wang, Y.; Du, Q.; Shao, G. 3D hierarchical network NiCo<sub>2</sub>S<sub>4</sub> nanoflakes grown on Ni foam as efficient bifunctional electrocatalysts for both hydrogen and oxygen evolution reaction in alkaline solution. *Int. J. Hydrogen Energy* **2017**, *42*, 25267–25276. [[CrossRef](#)]
57. Yin, X.; Sun, G.; Song, A.; Wang, L.; Wang, Y.; Dong, H.; Shao, G. A novel structure of Ni-(MoS<sub>2</sub>/GO) composite coatings deposited on Ni foam under supergravity field as efficient hydrogen evolution reaction catalysts in alkaline solution. *Electrochim. Acta* **2017**, *249*, 52–63. [[CrossRef](#)]
58. Du, C.; Yang, L.; Yang, F.; Cheng, G.; Luo, W. Nest-like NiCoP for Highly Efficient Overall Water Splitting. *ACS Catal.* **2017**, *7*, 4131–4137. [[CrossRef](#)]
59. Garrick, T.R.; Diao, W.; Tengco, J.M.; Stach, E.A.; Senanayake, S.D.; Chen, D.A.; Monnier, J.R.; Weidner, J.W. The Effect of the Surface Composition of Ru-Pt Bimetallic Catalysts for Methanol Oxidation. *Electrochim. Acta* **2016**, *195*, 106–111. [[CrossRef](#)]
60. Miao, K.; Luo, Y.; Zou, J.; Yang, J.; Zhang, F.; Huang, L.; Huang, J.; Kang, X.; Chen, S. PdRu alloy nanoparticles of solid solution in atomic scale: outperformance towards formic acid electro-oxidation in acidic medium. *Electrochim. Acta* **2017**, *251*, 588–594. [[CrossRef](#)]
61. Wang, W.; Lei, B.; Guo, S. Engineering Multimetallic Nanocrystals for Highly Efficient Oxygen Reduction Catalysts. *Adv. Energy Mater.* **2016**, *6*, 1600236. [[CrossRef](#)]
62. Gong, K.; Du, F.; Xia, Z.; Durstock, M.; Dai, L. Nitrogen-Doped Carbon Nanotube Arrays with High Electrocatalytic Activity for Oxygen Reduction. *Science* **2009**, *323*, 760–764. [[CrossRef](#)] [[PubMed](#)]
63. Dai, L.; Xue, Y.; Qu, L.; Choi, H.-J.; Baek, J.-B. Metal-Free Catalysts for Oxygen Reduction Reaction. *Chem. Rev.* **2015**, *115*, 4823–4892. [[CrossRef](#)] [[PubMed](#)]
64. Wang, L.; Tang, Z.; Yan, W.; Yang, H.; Wang, Q.; Chen, S. Porous Carbon-Supported Gold Nanoparticles for Oxygen Reduction Reaction: Effects of Nanoparticle Size. *ACS Appl. Mater. Interfaces* **2016**, *8*, 20635–20641. [[CrossRef](#)] [[PubMed](#)]

